Tannin-based resins for 3D printing of porous carbon architectures

Pauline Blyweert, Nicolas Vincent, Jan Macutkevic, Vanessa Fierro, Alain Celzard

Tannin-based resins for 3D printing of porous carbon architectures

Pauline Blyweert †, Vincent Nicolas †, Jan Macutkevic‡ ,

Vanessa Fierro †, Alain Celzard †,[*]

† Université de Lorraine, CNRS, IJL, F-88000 Epinal, France

‡ Faculty of Physics, Vilnius University, Sauletekio 9, LT-10222 Vilnius, Lithuania

[*]Corresponding author: Pr. Alain Celzard (alain.celzard@univ-lorraine.fr), Université de Lorraine

KEYWORDS

Tannin, Porous carbon, Stereolithography, Additive manufacturing

ABSTRACT

Carbon structures, unlike metals or polymers, can hardly be directly implemented in additive manufacturing, and their sustainable nature is extremely limited. In this work, we demonstrate that porous carbon structures can be obtained by laser stereolithography of acrylate-tannin mixed resins, followed by a pyrolysis step. By adjusting the initial acrylate / tannin ratio in the resin, the density and volume shrinkage of the resultant carbon, and consequently the mechanical properties of the corresponding carbon-based architectures, could be modified. The moderate electrical conductivity of the structures, reaching about 7 $S.cm^{-1}$, and their broadband absorption in microwaves open up possibilities for electrochemical or electromagnetic applications. Thus, the possibility of obtaining complex free-standing structures with imperceptible warpage, low volume shrinkage, and adjustable density offers an opportunity to develop 3D-printed carbon materials with a significant proportion of bio-based precursors, which can be easily adapted for a large number of applications.

INTRODUCTION

Porous carbon materials, thanks to their excellent chemical stability and unique mechanical, electrochemical, thermal and electrical properties [1,2], are used in many industrial processes such as heat management [3], gas storage [4], electrochemical energy storage and conversion [5,6], among others. Given their central role, it would make sense to find a fast, inexpensive and accurate way

to produce tailored complex systems, not only to broaden the application range of these materials, but also to give them a more ecological character. This versatility can be achieved with 3D printing methods [7], and especially by vat photopolymerisation, one of the most accurate technologies [8,9]. Nevertheless, since pure carbon cannot be melted, sintered or polymerised, this particular element is not directly applicable in additive manufacturing. Thus, most 3D-printed carbon materials are obtained by printing a carbon precursor, followed by a pyrolysis step.

Existing studies have reported the printing of porous carbon through stereolithography technology using commercial or custom resins, followed by a pyrolysis step. These approaches have allowed for the realisation of highly porous carbon materials with tailored pores in a reduced number of steps [10–13]. Nevertheless, in most cases, the printed resin had a low carbon yield [14,15] and underwent significant volume shrinkage (50 – 90%). Besides, the photocurable or thermosets resins [16] used in those approaches are all of petrochemical origin. To make 3D-printed porous carbons more sustainable, it is therefore interesting to use bio-based resins as carbon precursors. Unlike previous studies in which bio-based carbon precursors such as lignin, cellulose or monosaccharides have been used in Direct Ink Writing technology [17–19], in this work we present an approach to print highly porous carbons with low shrinkage and warpage from bio-based photoresin using laser stereolithography.

This approach consists of adding a wood extract, condensed (mimosa) tannin, to the photocurable resin to build complex structures and then converting the latter into carbon through a pyrolysis step. Indeed, mimosa tannin is an abundant phenolic bioresource with a carbon yield on pyrolysis of about 47%, which has been widely studied over the years to synthesise a wide range of carbon structures [20]. Herein, we show for the first time the possibility of printing a tannin-based resin to ensure high carbon yield with low shrinkage upon carbonisation, and we

discuss some properties of these new materials based on rheological, structural and physical characterisation.

EXPERIMENTAL SECTION

Materials

Hexanediol diacrylate (HDDA, SR238), pentaerythritol tetraacrylate (PETA, SR295) and acrylate oligomer (CN154 CG) were kindly supplied by Sartomer (Arkema Group, France). Bis(2,4,6-trimethylbenzoyl)phenylphosphine oxide (BAPO) was supplied by Lambson (Arkema Group, England). Mimosa (*Acacia Mearnsii*) tannin extract, a light-brown powder containing 80-82% phenolic material based on flavonoid units, commercially available under the name Fintan OP, was kindly provided by SilvaChimica (St Michele Mondovi, Italy) and used as a bio-based carbon precursor. All products were used as received without further purification.

Preparation of tannin-acrylate resins, 3D printing and pyrolysis

A BAPO photoinitiator (content 0.30 wt.%) and the acrylates monomers (SR238, SR295 and CN154 CG), added in the proportions shown in Table S1, were mixed thoroughly at 50 °C for 20 min to obtain a homogeneous resin. Then, a fixed amount of tannin was added and mixed by hand to the acrylate resin to obtain tannin-acrylate resin with a tannin content of 0, 10, 20, 25 or 30 wt.%. The corresponding formulations and printed structures were named T-0, T-10, T-20, T-25 and T-30, respectively, and the derived carbons were called CT-0, CT-10, CT-20, CT-25 and CT-30, respectively.

A commercial desktop SLA (λ = 405 nm, DWS J28, DWS, Italy) was employed to print 3D structures from tannin-acrylate resins. After the printing procedure, the structures were removed

from the build platform and rinsed twice in an isopropanol bath for 10 min to remove uncured resin. Afterwards, the products were post-cured in a UV oven (λ = 405 nm) for 20 min at room temperature.

The printed meshes were finally converted into carbon materials under pure nitrogen (flow rate 100 mL·min^{-1}) in a tubular furnace with a heating rate of 1.5 °C·min^{-1} to 400 °C, then a 20 min step at 400 °C, followed by a second ramp of 2.5 °C min^{-1} up to the final temperature of 900 °C, which was maintained for 1 hour (Figure 1). This particular temperature program was chosen to stabilise the architectures during thermal degradation.

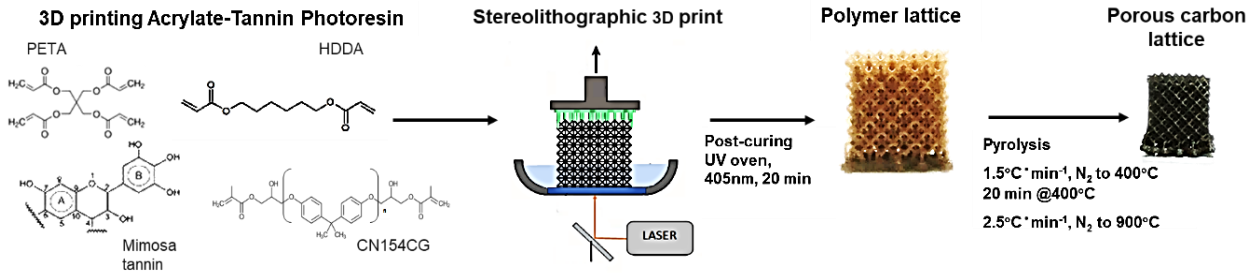

Figure 1. Schematic illustration of the fabrication strategy for 3D-printed tannin-based carbon materials.

Characterisation

Materials characterisation

A Brookfield DVII+ PRO viscometer with cone-plate geometry (spindle CPE-51, gap 0.013 mm) was used to measure the viscosity of the resins at room temperature.

The volume-based particle size distribution of the tannin powder was measured using a laser diffraction particle size analyser (Mastersizer 3000, Malvern), equipped with an automated dry powder dispersion unit (Aero S, Malvern). The powder was dried before measurements.

Thermogravimetric analysis (TGA) coupled with Differential Scanning Calorimetry (DSC) was performed using an STA 449 F3 Jupiter® apparatus (Netzsch) and provided access to the carbon yield (ratio of the weight of carbon after pyrolysis to the weight of the initial resin) and glass transition temperature of the different resins, respectively. Cured resin samples (~ 10mg) were tested from 30 to 800 °C with a heating rate of 10 °Cmin^{-1} under argon flow. The argon flow was then replaced by air to deduce the ash content.

Elemental analysis (EA) of the resultant carbon materials was performed in an Elementar Vario EL Cube analyser.

Structure, porosity, and textural properties of carbon materials

The linear shrinkage was calculated using Eq. (1), where the dimension can be height, thickness or length of the printed architectures. The data reported are the average values of at least 5 measurements on 3 samples obtained from each carbon type.

$$Shrinkage\ (\%) = \frac{Dimension\ before\ \ pyrolysis - Dimension\ after\ prolysis}{Dimension\ before\ pyrolysis} \times 100 \quad (1)$$

Scanning Electron Microscopy (SEM) and Energy-dispersive X-ray spectroscopy (EDX) were performed with a Zeiss GeminiSEM 360 microscope. Transmission Electron Microscopy (TEM) images were obtained using a JEM ARM 200F Cold FEG TEM/STEM operating at 200 kV, using spherical aberration (Cs) probe and image correctors. The samples were prepared by dispersing carbon powder in ethanol, after which a single drop of the suspension was deposited on a carbon-coated copper grid (200 mesh).

X-ray diffraction (XRD) was carried out using a Panalytical X'Pert Pro diffractometer in a Bragg-Brentano configuration in reflection with a Cu anode.

Raman spectra were recorded with a Horiba XploRa Raman apparatus equipped with a 50× long-range objective (wavelengths of 532 and 638 nm, filtered at 10% of their maximum energy). The spectra obtained at a wavelength of 638 nm were then fitted by the method described by Mallet-Ladeira et al. [21] using a double Lorentzian for the D band and an asymmetric mixed Gaussian-Lorentzian profile for the G band.

The bulk density ($\rho_{b,}$ g cm^{-3}) was calculated from the measured mass and volume of three samples of each carbon type obtained. The skeletal density ($\rho_{s,,}$ g cm^{-3}) was determined by helium pycnometry using an Accupyc II 1340 (Micromeritics) automatic apparatus, averaging 30 measurements. Sample were ground and dried before each measurement. The total porosity, Φ (dimensionless), was then calculated according to Eq. (2):

$$\Phi = 1 - \frac{\rho_b}{\rho_s} \quad (2)$$

N_2 and H_2 adsorption experiments at -196°C were carried out with a Micromeritics 3-flex automatic adsorption apparatus. Samples (~ 1 g) were degassed under vacuum before analysis for at least 48h at 200 °C. The Brunauer-Emmett-Teller [22,23] (BET) method was applied to N_2 isotherms to obtain the BET area (A_{BET}). Pore size distribution (PDS) and total surface area (S_{NLDFT}) were calculated from the combination of N_2 and H_2 adsorption isotherms using a two-dimensional non-local density functional model (2D-NLDFT) available in SAIEUS software (Micromeritics [24]).

Mercury intrusion was performed using a Micromeritics AutoPore IV 9500 up to a pressure of 414 MPa.

Physical properties of carbon materials

The electrical conductivity σ (S cm^{-1}) was measured by the four-point method using a Keithley 6430 source-measure unit on 3D-printed and then pyrolysed 2 mm × 2 mm × 15 mm parallelepipeds. The electrical conductivity was calculated according to:

$$\sigma = \frac{2\,I}{(|V^+| + |V^-|)}\frac{L}{S} \quad (3)$$

where V^+ and V^- are the voltage values (V) measured with the current I (A) flowing in one direction and then in the other, so as to correct the measurements for a slight thermoelectric effect that is always present. S (cm²) is the cross-sectional area and L (cm) is the distance between the two opposite sides on which the electrical contacts were placed. The electrical conductivity of the conductive skeleton, σ_s, was calculated with Eq. (4), which is a good approximation for rigid open-cell foams with node effects [25,26]. This equation was preferred to others corresponding to closed porosity, because polymeric precursors produce a significant amount of gases during pyrolysis and hence a totally open porosity, as already proved by the mercury intrusion experiments (see below):

$$\sigma_S = \frac{3\sigma}{\left[(1-\Phi)+2(1-\Phi)^{\frac{3}{2}}\right]} \quad (4)$$

Microwave measurements in the 24-39 GHz (Ka-band) frequency range were carried out with an ELMIKA R2-408R scalar network analyser. The samples were placed directly in a 7.2 × 3.4 mm cross-section waveguide, perpendicular to the wave propagation, and the modules of the amplitude of transmitted (S_{21}) and reflected (S_{11}) signals were measured. From these data, the (dimensionless) coefficients of reflection (R), transmission (T) and absorption (A) were calculated according to Eq. (5):

$$R = {S_{11}}^2$$
$$T = {S_{21}}^2 \quad (5)$$
$$A = 1 - {S_{11}}^2 - {S_{21}}^2$$

Mechanical properties of the different 3D printed carbon were investigated by quasi-static compression using an Instron 5944 universal testing machine equipped with a 2 kN load cell. The compression tests were carried out in triplicate at a constant load rate of 2 mm·min^{-1}.

More details of sample preparation and methods are given in the Supplementary Information.

RESULTS AND DISCUSSION

Rheological properties and thermal behaviour of the resins

In stereolithography, the viscosity of the resin is a crucial parameter. In most cases, a viscosity of less than 3 Pa·s (at the printing temperature and a shear of about 100 s^{-1}) is desired to promote recoating and self-levelling of the resin [27,28]. The viscosity of uncured acrylate-tannin resins with a tannin content between 10 and 30 wt.% was determined as a function of shear rate in a region of 10 to 200 s^{-1} (Figure 2a). At higher tannin contents, the resultant resins were in the form of a paste that cannot be used in a stereolithography apparatus.

The unfilled resin (here referred to as T-0) showed Newtonian behaviour with a viscosity of about 1.0 Pa·s at a shear rate of 100 s^{-1}. It turns out that Mimosa tannin is not soluble in the acrylate resin, and is therefore dispersed in it in the form of solid particles with an average diameter of 54.5 µm, according to measurements made with the Mastersizer (Figure S1). It is well established that, due to particle interactions, the viscosity of suspensions increases with the volume concentration of solids [29]. Thus, as expected, the viscosity increased with the tannin content (Figure 2b). For all filled resins, shear-thinning behaviour in the low-shear rate region (below 10 s^{-1}) was observed, with viscosity decreasing to a steady state (tending towards 1.3 Pa·s)

at high shear rates. This observation, typical of highly particle-loaded suspensions, can be explained by the variable interparticle and particle-fluid interactions under shear [30–34]. As the shear stress increases, immobilised acrylate chains are indeed released, and the friction between tannin particles decreases. Therefore, from a macroscopic point of view, the viscosity decreases as seen in Figure 2a. Due to the initial viscosity of the acrylate resin, the suspension of tannin particle remains stable during the printing processes (and even for weeks at room temperature), which limits the heterogeneity of the final structure.

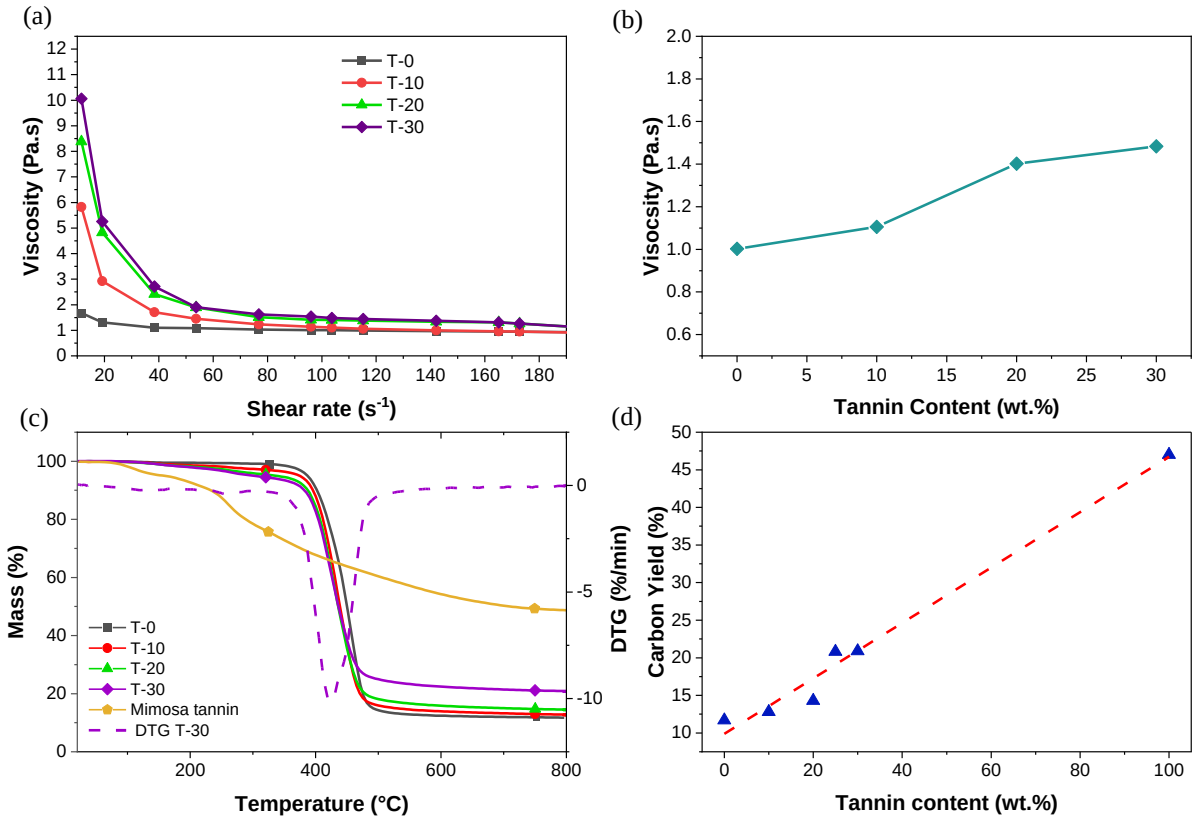

Figure 2. (a) Viscosity versus shear rate of acrylate resins containing different weight fractions of tannin (from 0 wt.% in T-0 to 30 wt.% in T-30). (b) Viscosity of acrylate resin at a shear rate of 100 s^{-1} as a function of tannin content. (c) TGA (mass loss) curves, under argon and up to 800 °C, of the same acrylate resins as in (a); that of pure tannin is given for comparison, and the DTG

curve is provided as a guide for sample T-30 only, as the others DTG curves are similar. (d) Carbon yield at pyrolysis as a function of initial tannin content; the value corresponding to a resin with 25 wt.% tannin was also added.

The temperature behaviour of the acrylate-tannin resin was evaluated by TGA and the corresponding differential curves (DTG) (Figure 2c). The UV-cured acrylate resin without tannin started to lose weight at about 320 °C and degraded to char by 680 °C with a mass loss of about 85%. This degradation corresponds to the depolymerisation of acrylates at high temperature as well as to the random radical scission of the free linear chains, leading to volatile chain fragments, including ethylene and methane, the quantitative yield of which depends on the stability of the radicals formed but also on side-chain reactions (side group elimination or rearrangement) [35–37]. In the presence of tannin, three regions of mass loss were clearly identified [38]. The first region is located between 30 and 170 °C, with a DTG peak around 132 °C, and corresponds to the evaporation of absorbed water and the formation of small volatile compounds (CO, CO_2) released at the beginning of tannin degradation. The second region between 170 and 310 °C, with a DTG peak around 260 °C, is due to the degradation of tannin and acrylate resin. Finally, the decomposition of the rigid segments of the resin and the formation of carbon material occur between 310 and 680 °C. As expected, the addition of tannin significantly increased the final carbon yield at 800 °C, from 11.7 to 20.8 % for the samples with 0 wt.% and 30 wt.% of tannin, respectively. The carbon yield increased linearly with the weight fraction of tannin, as shown in Figure 2d, where the carbon yield of pure tannin (47 %) has been plotted. In addition, for all samples, the ash content remained below 0.5 wt.%.

Morphology and composition of printed carbon structures

Tetrakaidecahedra meshes (Figure 3a, wall size of 200 µm) and solid cubes were printed from 30 µm-thick layers. After pyrolysis, the colour of the samples changed from light brown to bright black for the acrylate resin without tannin to matte black for the CT-30 structure (Figure 3b).

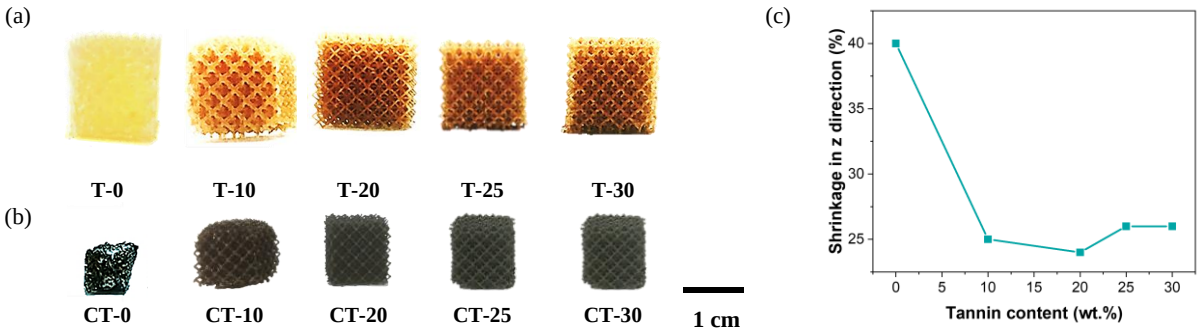

Figure 3. 3D-printed structures: (a) before and (b) after pyrolysis, with various tannin contents increasing from left to right (formulations T-0, T-10, T-20, T-25 and T-30); (c) Linear shrinkage of the structures after pyrolysis in *z*-direction (printing direction) as a function of tannin content.

The addition of tannin to the formulation was found to have an effect on the structure shrinkage as evidenced in Table S2. The samples with tannin, regardless of their architecture, tended to shrink linearly by 25% in each direction, while the tannin-free structure shrank by 40% in the *z*-direction and by 30% in *x*-*y* directions with warpage. The shrinkage phenomenon results from the evolution of volatile matters during carbonisation. During the pyrolysis process, the acrylate polymer matrix is progressively heated to temperatures above its glass transition temperature (found to be 126 °C by DSC measurement for the pristine resin, and reduced to 115 °C for the T-25 resin due to polymer/particles interactions [39,40], Figure S2) and enters a more flexible state subject to deformation. As the tannin degrades significantly less than the resin and loses much less weight, even at much higher temperatures (Figure 2c), it stabilises the structure during this plastic state and thus reduces warpage in different directions.

SEM images of carbon structures CT-0 and CT-30 are presented in Figure S3 and Figure 4. Rather smooth surfaces with a few craters allowing gases formed during the pyrolysis step to escape were observed on all structures (Figure S3). In contrast, SEM images after fracturing (Figure 4) revealed extensive internal porosity with many large oval bubbles in the CT-0 structure, while narrower pores can be seen on the CT-30 carbon architecture. EDX results (not shown) evidenced similar carbon and oxygen composition for each sample.

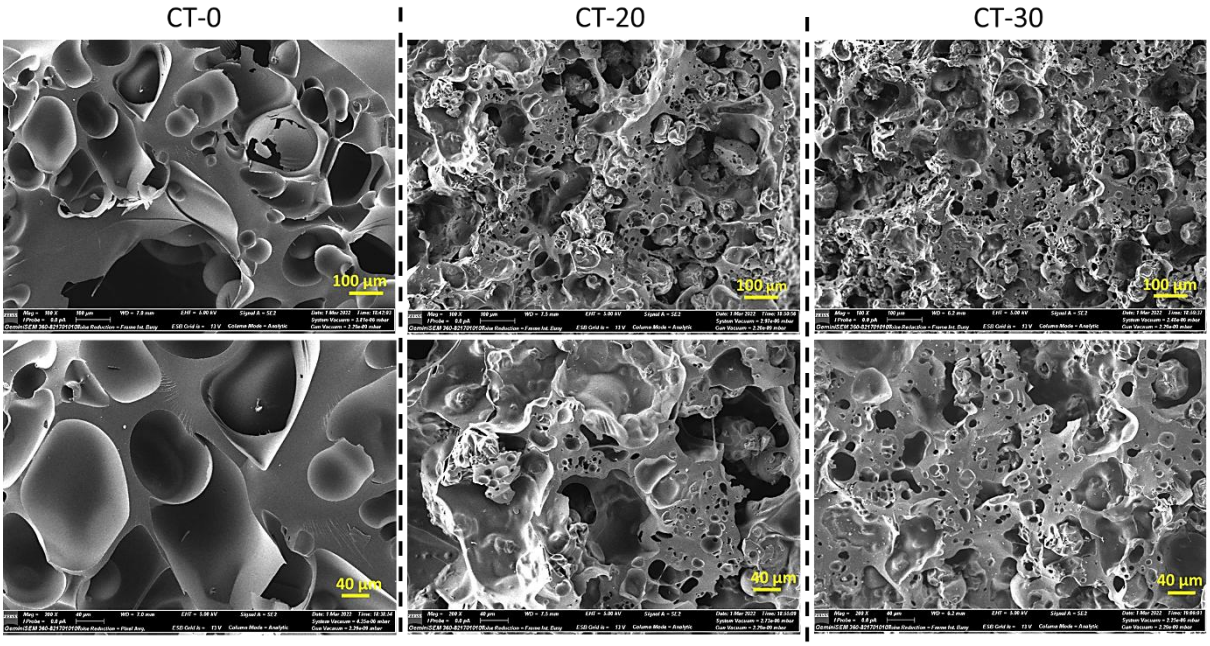

Figure 4. SEM images of a fractured area of CT-0, CT-20 and CT-30 samples of 3D-printed structures. Scale bars: 100 µm (top row), and 40 µm (bottom row).

Table S3 presents the bulk chemical composition of the different 3D-printed carbons. The nitrogen (N) content is very low and no sulphur (S) was detected, while oxygen (O) is present in significant amounts in the carbon structures. These measurements are in agreement with the composition of other carbons based on Mimosa tannin [20,41], as no doping treatment was carried out on these materials. Given the usual uncertainties on this kind of analysis, it is difficult to

consider that the samples are really different in terms of composition, and we can assume that all of them have C, H, N, S and O contents of about 95, 1.3, 0.3, 0 and 3.5 wt.%, respectively. The differences between the samples do not show any clear trend, and can be attributed to inhomogeneities, despite the repetitions and calculated averages.

Structural properties of printed carbon structures

TEM observations were performed to investigate the nanostructure of the carbon materials (Figure S4). At high magnification, TEM evidenced a highly disordered structure in all samples, which was expected from a phenolic precursor in the absence of graphitisation catalyst [20]. High-resolution images and the presence of a well-defined halo seen by Fast Fourier Transform (FFT) also revealed the existence of very small lamellar domains dispersed in a highly disordered matrix.

Figure 5a shows the Raman spectra obtained at a wavelength of 532 nm, *i.e.*, with a green laser, which corresponds to the vast majority of carbon spectra reported in the literature. They are completely typical of highly disordered carbons, as expected from the precursors used [20]. Indeed, at first order, the D-band, whose maximum is around 1350 cm^{-1}, is very broad with a shoulder around 1170 cm^{-1}, and the G-band, centered around 1600 cm^{-1}, is just a little less broad. The intensity ratio of the D/G bands is very close to 1, and at second order, the profile between 2200 and 2700 cm^{-1} is not structured. The spectra are very similar from one formulation to the other, especially when tannin is present. The carbon obtained with the formulation without tannin differs very slightly from the others by its somewhat shallower valley between the D and G bands. Moving from sample CT-0 to sample CT-30, the D/G intensity ratio increases very slightly, from 1.01 to 1.04. Considering the very disordered and non-graphitizable character of these carbons,

this evolution corresponds to a slight increase in the size of the coherent domains, measured through the $L_{a,Raman}$ parameter.

Figure 5b shows the first-order spectra, now obtained with the 638 nm laser, *i.e.*, with a red laser, at the wavelength of which equation (S2) applies. As expected, the D band has moved to lower Raman shifts, around 1320 cm^{-1}, while the G band has remained fixed. The D/G intensity ratios also increased, but the trend remained the same, with values increasing from 1.13 to 1.16 for samples CT-0 and CT-30, respectively. Figure 5d shows the fit of these two extreme samples by the method described in [21]. The fits provided the half-widths at half maximum of the G band, which decreased from 59.5 cm^{-1} for CT-0 to 55.2 cm^{-1} for CT-30, with which the values of $L_{a,\ Raman}$ could be calculated from Eq (S2). The corresponding values and their uncertainties are given in Figure 5c. On average, $L_{a,\ Raman}$ thus increases from 1.6 to 2.5 nm, and the three formulations containing tannin gives values very close to each other. Such small values definitely confirm that these carbons are highly disordered and not graphitizable.

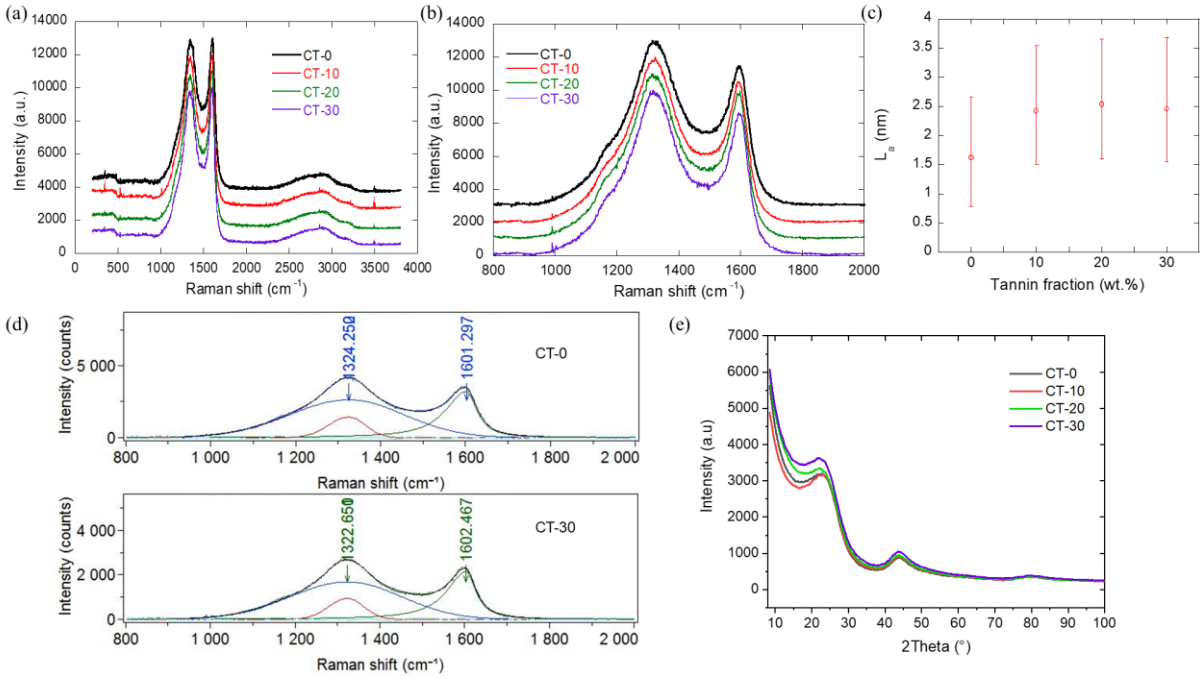

288

289 Figure 5. Raman spectra and XRD patterns of 3D-printed carbon structures for various initial
290 acrylate / tannin ratios: (a) Full spectra obtained at a wavelength of 532 nm; (b) First-order
291 spectra obtained at a wavelength of 638 nm. In (a) and (b), the spectra have been shifted with
292 respect to each other along the intensity axis (whose units are arbitrary) to better distinguish them;
293 (c) Changes of $L_{a,\,Raman}$ with the tannin content in the formulation; (d) Fits of the spectra shown in
294 (b) according to the method detailed in [21]; (e) XRD patterns.

295 The XRD patterns are shown in Figure 5e. As expected, the XRD profile was nearly the same
296 for all samples, with the *002* reflection appearing as a broad band with a maximum at Bragg
297 angle 2θ of 20-24°. The presence of such a broad reflection confirmed the existence of crystalline
298 carbon nano-domains in a highly disordered carbon matrix, as expected from the observation in
299 the high-magnification TEM images. Bands *10*λ (2θ = 44°) and *11*λ (2θ = 80°) appeared as broad
300 and low-intensity reflections, which is indeed typical of disordered carbon. This is further
301 confirmed by the corresponding values of $L_{a,\,XRD}$, calculated from Eq. (S1), which are extremely

low, around 2 nm for all samples. These values are in agreement with those calculated above by Raman spectrometry. Finally, the high intensities observed at low angles indicate the presence of microporosity.

Textural properties of printed carbon structures

The bulk density of the 3D-printed structures after carbonisation depends on the acrylate / tannin ratio (Table S4). The carbonaceous material obtained from the pure acrylate resin was denser (0.442 g cm^{-3}) than its counterparts derived from tannin-acrylate mixed resins, with bulk density values ranging from 0.305 to 0.408 g cm^{-3} when the tannin content in the formulation increased from 10 to 30 wt.%. This difference can be explained by the significant linear shrinkage observed with sample CT-0 (40 % in the *z*-direction), compared to the other samples with an average shrinkage of 25 % (in the *z*-direction) (see again Table S2). In contrast, the carbon skeletal densities remained the same, within the standard deviation, for tannin content between 0 and 30%, with an average value of 1.80 g cm^{-3}. The high total porosity, ranging from 76 to 83 %, is mainly due to the depolymerisation of acrylates and the gas released during transformation of tannin upon pyrolysis.

The influence of tannin content on the pore structure after pyrolysis, was studied. Figure 6 shows the N_2 and H_2 adsorption-desorption isotherms, from which the textural properties of CT-20, CT-25 and CT-30 were calculated. The outgassing of samples CT-0 and CT-10 was too long, which indicates extremely narrow porosity preventing any correct adsorption measurement. We therefore report results for only 3 of the 5 carbon structures, which are given in Table S4. Figure 6a shows type Ia nitrogen adsorption-desorption isotherms, characteristic of microporous materials with predominantly narrow (width less than ~ 1 nm) micropores, following the IUPAC

classification [23]. All three isotherms exhibited a low-pressure hysteresis that it is due to slow desorption in these very narrow pores. The amount of nitrogen and hydrogen adsorbed increased with the amount of tannin added, although the largest increase was observed for CT-25 when compared with CT-20, and slight differences were found between CT-25 and CT-30. Therefore, the textural properties increased with the amount of tannin added, and thus A_{BET} varied from 265 to 375 $m^2 \cdot g^{-1}$ while S_{NLDFT} varied from 850 to 910 $m^2 \cdot g^{-1}$ (Figure 6c). These large differences between A_{BET} and S_{NLDFT} are due: first, to the fact that the BET method underestimates the surface area when a significant portion of the pores are smaller than 0.7 nm in diameter; secondly, to the fact S_{NLDFT} was calculated using N_2 and H_2 adsorption isotherms together, and the diameter of the H_2 molecule is about 0.3 nm while that of N_2 is about 0.35 nm. Therefore, H_2 has access to porous surface that N_2 cannot penetrate. The corresponding isotherms are presented in Figure 6b.

Figure 6d shows that the three materials had very similar PSDs, the main difference being a slight increase in pores around 0.7 nm when increasing the percentage of tannin from 20 to 25%. Figure 6e shows the corresponding cumulative pore volumes. The total pore volumes, V_T, were relatively low, between 0.20 and 0.23 $cm^3\ g^{-1}$ (see Figure 6f), and mostly composed of micropores. Only CT-30 had a few mesopores (pore diameter between 2 and 50 nm) but in almost negligible amount, 0.01 $cm^3\ g^{-1}$ (thus not shown in Table S4). Most of the micropores, 75% for CT-20 and 65% for CT-30, were in the ultramicropore range, and their average diameter was 0.58 ± 0.2 nm. The latter means that only H_2 molecules are able to form a bilayer inside pores with a diameter of about 0.6 nm, and thus provides insight into the large difference between A_{BET} and S_{NLDFT}. The fraction of micropores where the H_2 bilayer cannot be formed, corresponding to diameters smaller than 0.5 nm, is still remarkable and varies from 65 to 59% for CT-20 and CT-30, respectively.

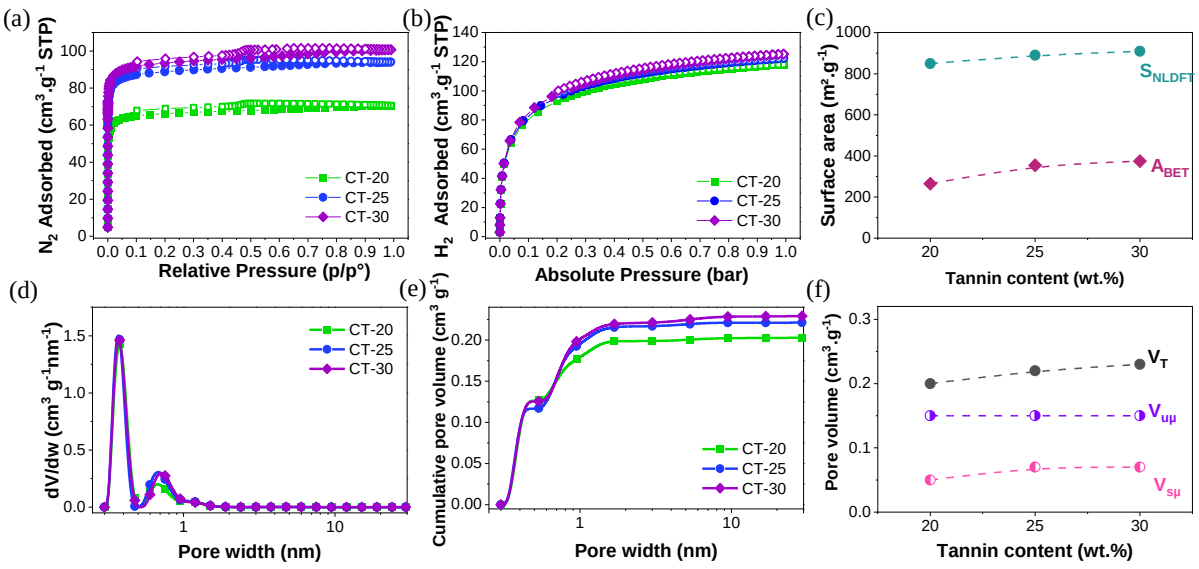

347

348 Figure 6. (a) Nitrogen; and (b) hydrogen adsorption (full symbols) – desorption (empty symbols)
349 isotherms; (c) BET area and NLDFT surface area of the printed carbons as a function of initial
350 tannin content; (d) pore size distributions; (e) cumulative pore volumes calculated by the 2D-
351 NLDFT model; and (f) pore volumes as a function of initial tannin content.

352 Raw and differential mercury intrusion curves plotted as a function of pressure and pore
353 diameter, respectively, are presented in Figure S5. Analysis of meso/macropores structure by
354 mercury porosimetry confirmed that most of the pore volume can be attributed to large pores with
355 a distribution centred on a diameter of about 10 µm, as observed in the SEM images. All pore
356 size distribution (PSDs) were very broad and rather multimodal, with pore diameters covering
357 three orders of magnitude. The addition of tannin to the initial resin was found to shift the median
358 pore diameter (calculated with Eq. S3) to lower values as the density increased, from 14 µm for
359 CT-0 to 5 µm for CT-30.

360 The average pore diameters were significantly higher than those reported for other 3D-printed
361 carbon monoliths prepared by stereolithography in the presence of porogens, followed by

oxidation and pyrolysis steps, which exhibited typical pore diameters (d_{90}) between 30 and 70 nm (but not including pores larger than 10 µm in diameter) [12]. However, they were similar to those of pyrolytic carbon electrodes derived from SLA technology with pore diameters of about 10 µm [11] and to those of tannin-derived monoliths prepared by emulsion templating, with values between 1 and 10 µm [42,43]. This is an important result because, unlike the latter materials, no particular synthesis strategy was used here to obtain pores of these dimensions in such large numbers. This result also indicates that this porosity is both wide and connected, and that it is therefore easy to develop, by classical activation processes, the micro- and mesoporosity observed above by gas adsorption. It should therefore be possible to obtain monolithic, architecturally structured activated carbons, useful for example as highly permeable, rigid and easy-to-handle catalyst supports, unlike granular or powdered carbons.

Physical properties of printed carbon structures

The electrical conductivity of a carbon structure may vary greatly as a function of texture, which in turn is a function of precursor and heat treatment temperature, and also somewhat as a function of the relative density of the material. Since the skeletal density and porosity of the different 3D-printed carbons are similar (see again Table S4), their electrical conductivity was assumed to remain of the same order of magnitude. Indeed, Table S5 shows values between 6.05 and 7.1 S cm^{-1} for the different formulations. Similarly, the solid electrical conductivity, *i.e.*, the electrical conductivity excluding the sample porosity, calculated using Eq. (4), was found to be between 43 and 59 $S \cdot cm^{-1}$. This narrow range of values is reasonable considering the approximations made to obtain Eq. (4) on the one hand, and is moreover typical of glassy carbon on the other hand, for which values of 11 $S \cdot cm^{-1}$ [44] to 70 $S \cdot cm^{-1}$ [45] have been reported.

These relatively modest conductivity values are of great interest, as 3D-printed carbonaceous architectures with low to medium conductivity struts have recently been shown to produce broadband photonic crystals in the GHz range, while higher conductivities combined with the same architectures result in higher absorption coefficients, but in an incomparably narrower frequency range [46]. To prove this, printed CT-25 parallelepipeds with final dimensions of 7.1 × 3.3 × 2 mm were analysed in the Ka band.

In the whole range of frequencies studied, the EM response is strongly dominated by the reflection, whose coefficient varies typically between 0.7 and 0.8. As a result, the absorption coefficient varies between roughly 0.2 and 0.3, and the transmission is almost zero (Figure 7). Analysis of the data collected yielded the shielding effectiveness, $SE = -20 \log(S_{21})$, and it can be concluded that the studied material provide a shielding level in the range of 20 to 22 dB. Although it is not very high, it is indeed a broadband absorption, which can be interesting to build photonic crystals and thus brings new perspectives to these porous biosourced carbons.

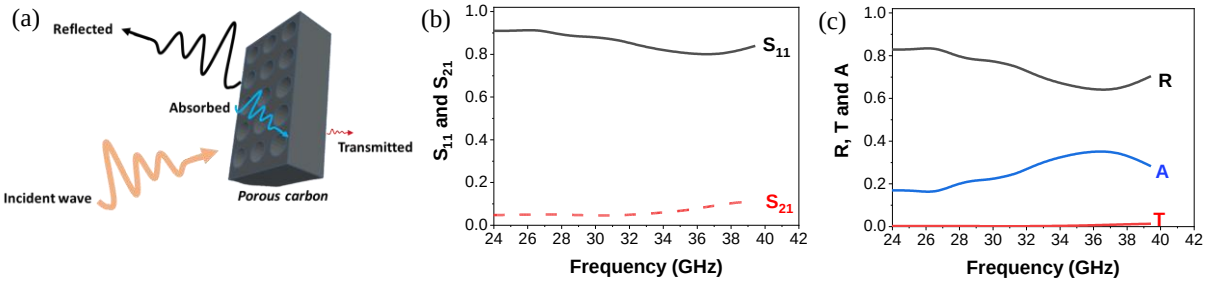

Figure 7. Electromagnetic properties of the CT-25 structure: (a) schematic of the EM response; (b) frequency dependence of the *S* parameters ; (c) corresponding behaviour of the reflection, transmission and absorption coefficients.

The strain-stress compression curves of 3D-printed carbon cubic samples are given in Figure S6a-S6e. The compressive strength was defined as the highest stress at the first peak, the slope of

403 which was used to determine the Young's modulus. Following this first peak, the stress decreased
404 sharply, indicating a brittle failure of the material. The repetition of this phenomenon throughout
405 the compression of the samples led to serrated stress-strain characteristics explained by the
406 propagation of cracks in the carbon matrix. This behaviour then gave way to a progressive
407 densification of the material, as indicated by the increase in stress at strains above 35 %.

408 As expected, due to its denser structure obtained after pyrolysis (see again Table S4), the
409 sample printed with tannin-free acrylate resin showed relatively high compressive strength at
410 break (2.9 MPa) and high Young's modulus (156 MPa). These values decreased significantly to
411 1.4 MPa and 83 MPa, respectively, with the addition of 10 wt.% of tannin in the resin. This can
412 be explained by the decrease in density of the structures due to the low volume shrinkage
413 observed in the presence of tannin (Table S2). Then, due to this density gain, the mechanical
414 properties of the 3D-printed carbons increased with the increase of tannin content from 10 wt.%
415 to 30 wt.% to reach values close to those of the sample without tannin (CT-0), see Figure S6f and
416 Table S6. Because of the reduction in porosity with tannin loading from 10 to 30 wt.%, the
417 materials became more brittle, as indicated by the reduction in strain at break with values
418 decreasing from 7.0 to 2.8% (Table S6). In this printed system, tannin, being a bio-based carbon
419 precursor, helped to maintain the structure after pyrolysis and increase the material yield, but
420 only really appeared as a reinforcement at high loading. Under these conditions, at 30 wt.% of
421 tannin, mechanical properties are about equivalent to those of the carbonised pristine acrylate
422 resin, but with a significantly better yield and with a non-negligible share of renewable and
423 ecological material. Generally speaking, these mechanical properties are higher than those
424 obtained for carbon manufactured by stereolithography with a similar density [12].

425

CONCLUSION

The present paper demonstrated for the first time an effective strategy to develop 3D-printed carbon materials from bio-based resins using stereolithography (SLA). A new resin formulation based on an acrylate-tannin suspension was developed to meet the viscosity requirements for SLA printing. Indeed, despite its simple preparation and interesting mechanical properties, the shrinkage and warpage of the carbon structure derived from the pure acrylate resin remained significant and the carbon yield upon pyrolysis was low. Thus, the addition of tannin to the formulation allowed porous structures to be printed with an encouraging carbon yield close to 20 %. At a loading above 20 wt.%, tannin significantly reduced the warpage and volume shrinkage of the resulting carbon structures by about 35 %.

Increasing amounts of tannin were found to increase the bulk density of the structures while the skeletal density remained the same, leading to a high total porosity of about 80%. However, the non-graphitizable and very disordered carbon structures exhibited low surface area and wide pore size distribution, demonstrating the presence of a limited amount of very narrow pores together with very large pores with a median diameter ranging from 5 to 10 µm. These characteristics demonstrate the possibility of preparing architectured activated carbons, for instance for catalytic applications, as the pre-existing porosity can be further developed by conventional activation methods.

Theses carbon architectures also showed correct electrical conductivities in the range of 6-7 S cm^{-1}, varying with the textural properties, with a solid electrical conductivity between 43 and 59 $S \cdot cm^{-1}$, quite typical of glassy carbon. These properties open the way to the preparation of more sustainable 3D-printed devices for electrochemical applications, in which glassy carbon is widely used, but also for electromagnetic applications, for which moderate conductivities might be

preferable if broadband absorption is required. Finally, the new 3D-printed carbon structures presented here exhibited high mechanical properties with elastic-brittle behaviour. Nevertheless, in this system, tannin as a carbon precursor really appeared as a reinforcement only at high loading (> 25 wt.%).

The possibility of obtaining complex architectures with a non-negligible share of renewable and bio-based material, with good carbon yield and little shrinkage to tailor their properties, makes our approach promising for a broad range of applications. Thus, more detailed studies of such 3D carbon architectures will be carried out in the near future.

ASSOCIATED CONTENT

Supporting information: Additional experimental details and results including data and figures related to elemental analysis, porous texture, mechanical properties, particle size distribution of mimosa tannin, and SEM and TEM images of two different 3D-printed carbons.

AUTHOR INFORMATION

Corresponding Author

* Corresponding author. Tel: + 33 372 74 96 14. E-mail address: alain.celzard@univ-lorraine.fr (A. Celzard)

Funding Sources

This study was partially funded by ERDF [TALiSMAN project (2019-000214)]. This research received funding from Campus France and Lithuanian Science Council through the joint program PHC Gilibert #46414VC “Hybrid gels for electromagnetic applications”. It was also sponsored by the NATO Science for Peace and Security Program [Grant G5697 CERTAIN “Globular carbon-based structures and metamaterials for enhanced electromagnetic protection”].

ACKNOWLEDGMENT

P.B. acknowledges the French Ministry of Higher Education and the Grand-Est region for her PhD grant, resulting in the work presented herein. We thank Sartomer France and Elkem Silicone France for providing us materials. We also acknowledge the help from Christine Gendarme, François Montaigne and Jaafar Ghanbaja for SEM and TEM, Ghouti Medjahdi for X-ray diffraction, Rafael Luan Canavesi for gas adsorption, Alexander Zharov for electromagnetic properties and Philippe Gadonneix for technical assistance in the laboratory.

REFERENCES

(1) Muellen, K.; Feng, X. *Chemistry of Carbon Nanostructures*; De Gruyter: Berlin, Boston, 2017.

(2) Liu, H.; Wu, S.; Tian, N.; Yan, F.; You, C.; Yang, Y. Carbon Foams: 3D Porous Carbon Materials Holding Immense Potential. *J. Mater. Chem. A* **2020**, *8* (45), 23699–23723. https://doi.org/10.1039/D0TA08749A.

(3) Hu, L.; He, R.; Lei, H.; Fang, D. Carbon Aerogel for Insulation Applications: A Review. *Int J Thermophys* **2019**, *40* (4), 39. https://doi.org/10.1007/s10765-019-2505-5.

(4) Gatti, G.; Errahali, M.; Tei, L.; Cossi, M.; Marchese, L. On the Gas Storage Properties of 3D Porous Carbons Derived from Hyper-Crosslinked Polymers. *Polymers* **2019**, *11* (4), 588. https://doi.org/10.3390/polym11040588.

(5) Castro-Gutiérrez, J.; Díez, N.; Sevilla, M.; Izquierdo, M. T.; Ghanbaja, J.; Celzard, A.; Fierro, V. High-Rate Capability of Supercapacitors Based on Tannin-Derived Ordered Mesoporous Carbons. *ACS Sustainable Chem. Eng.* **2019**, *7* (21), 17627–17635. https://doi.org/10.1021/acssuschemeng.9b03407.

(6) Luo, X.; Chen, Y.; Mo, Y. A Review of Charge Storage in Porous Carbon-Based Supercapacitors. *New Carbon Materials* **2021**, *36* (1), 49–68. https://doi.org/10.1016/S1872-5805(21)60004-5.

(7) Blyweert, P.; Nicolas, V.; Fierro, V.; Celzard, A. 3D Printing of Carbon-Based Materials : A Review. *Carbon* **2021**, *183*, 449–485. https://doi.org/10.1016/j.carbon.2021.07.036.

(8) Quan, H.; Zhang, T.; Xu, H.; Luo, S.; Nie, J.; Zhu, X. Photo-Curing 3D Printing Technique and Its Challenges. *Bioactive Materials* **2020**, *5* (1), 110–115. https://doi.org/10.1016/j.bioactmat.2019.12.003.

(9) Ngo, T. D.; Kashani, A.; Imbalzano, G.; Nguyen, K. T. Q.; Hui, D. Additive Manufacturing (3D Printing): A Review of Materials, Methods, Applications and Challenges. *Composites Part B: Engineering* **2018**, *143*, 172–196. https://doi.org/10.1016/j.compositesb.2018.02.012.

(10) Bian, B.; Shi, D.; Cai, X.; Hu, M.; Guo, Q.; Zhang, C.; Wang, Q.; Sun, A. X.; Yang, J. 3D Printed Porous Carbon Anode for Enhanced Power Generation in Microbial Fuel Cell. *Nano Energy* **2018**, *44*, 174–180. https://doi.org/10.1016/j.nanoen.2017.11.070.

(11) Rezaei, B.; Pan, J. Y.; Gundlach, C.; Keller, S. S. Highly Structured 3D Pyrolytic Carbon Electrodes Derived from Additive Manufacturing Technology. *Materials & Design* **2020**, *193*, 108834. https://doi.org/10.1016/j.matdes.2020.108834.
(12) Steldinger, H.; Esposito, A.; Brunnengräber, K.; Gläsel, J.; Etzold, B. J. M. Activated Carbon in the Third Dimension—3D Printing of a Tuned Porous Carbon. *Adv. Sci.* **2019**, *6* (19), 1901340. https://doi.org/10.1002/advs.201901340.
(13) Wang, P.; Zhang, H.; Wang, H.; Li, D.; Xuan, J.; Zhang, L. Hybrid Manufacturing of 3D Hierarchical Porous Carbons for Electrochemical Storage. *Adv. Mater. Technol.* **2020**, *5* (6), 1901030. https://doi.org/10.1002/admt.201901030.
(14) Chen, X.; Zhao, G.; Wu, Y.; Huang, Y.; Liu, Y.; He, J.; Wang, L.; Lian, Q.; Li, D. Cellular Carbon Microstructures Developed by Using Stereolithography. *Carbon* **2017**, *123*, 34–44. https://doi.org/10.1016/j.carbon.2017.07.043.
(15) Szczurek, A.; Ortona, A.; Ferrari, L.; Rezaei, E.; Medjahdi, G.; Fierro, V.; Bychanok, D.; Kuzhir, P.; Celzard, A. Carbon Periodic Cellular Architectures. *Carbon* **2015**, *88*, 70–85. https://doi.org/10.1016/j.carbon.2015.02.069.
(16) Tian, X.; Zhang, W.; Li, D.; Heinrich, J. G. Reaction-Bonded SiC Derived from Resin Precursors by Stereolithography. *Ceramics International* **2012**, *38* (1), 589–597. https://doi.org/10.1016/j.ceramint.2011.07.047.
(17) Roman, J.; Neri, W.; Fierro, V.; Celzard, A.; Bentaleb, A.; Ly, I.; Zhong, J.; Derré, A.; Poulin, P. Lignin-Graphene Oxide Inks for 3D Printing of Graphitic Materials with Tunable Density. *Nano Today* **2020**, *33*, 100881. https://doi.org/10.1016/j.nantod.2020.100881.
(18) Shao, Y.; Guizani, C.; Grosseau, P.; Chaussy, D.; Beneventi, D. Use of Lignocellulosic Materials and 3D Printing for the Development of Structured Monolithic Carbon Materials. *Composites Part B: Engineering* **2018**, *149*, 206–215. https://doi.org/10.1016/j.compositesb.2018.05.035.
(19) Llamas-Unzueta, R.; Menéndez, J. A.; Suarez, M.; Fernández, A.; Montes-Morán, M. *3d Printed Porous Carbons by Direct Ink Writing of Whey*; SSRN Scholarly Paper 4074740; Social Science Research Network: Rochester, NY, 2022. https://doi.org/10.2139/ssrn.4074740.
(20) Celzard, A.; Fierro, V. "Green", Innovative, Versatile and Efficient Carbon Materials from Polyphenolic Plant Extracts. *Carbon* **2020**, *167*, 792–815. https://doi.org/10.1016/j.carbon.2020.05.053.
(21) Mallet-Ladeira, P.; Puech, P.; Toulouse, C.; Cazayous, M.; Ratel-Ramond, N.; Weisbecker, P.; Vignoles, G. L.; Monthioux, M. A Raman Study to Obtain Crystallite Size of Carbon Materials: A Better Alternative to the Tuinstra–Koenig Law. *Carbon* **2014**, *80*, 629–639. https://doi.org/10.1016/j.carbon.2014.09.006.
(22) Rouquerol, J.; Llewellyn, P.; Rouquerol, F. Is the Bet Equation Applicable to Microporous Adsorbents? In *Studies in Surface Science and Catalysis*; Llewellyn, P. L., Rodriquez-Reinoso, F., Rouqerol, J., Seaton, N., Eds.; Characterization of Porous Solids VII; Elsevier, 2007; Vol. 160, pp 49–56. https://doi.org/10.1016/S0167-2991(07)80008-5.
(23) Thommes, M.; Kaneko, K.; Neimark, A. V.; Olivier, J. P.; Rodriguez-Reinoso, F.; Rouquerol, J.; Sing, K. S. W. Physisorption of Gases, with Special Reference to the Evaluation of Surface Area and Pore Size Distribution (IUPAC Technical Report). *Pure and Applied Chemistry* **2015**, *87* (9–10), 1051–1069. https://doi.org/10.1515/pac-2014-1117.

(24) Jagiello, J.; Olivier, J. P. Carbon Slit Pore Model Incorporating Surface Energetical Heterogeneity and Geometrical Corrugation. *Adsorption* **2013**, *19* (2), 777–783. https://doi.org/10.1007/s10450-013-9517-4.
(25) Ashby, M. F.; Evans, A.; Fleck, N. A.; Gibson, L. J.; Hutchinson, J. W.; Wadley, H. N. G. *Metal Foams: A Design Guide*, 1st ed.; Boston, 2000.
(26) Cuevas, F. G.; Montes, J. M.; Cintas, J.; Urban, P. Electrical Conductivity and Porosity Relationship in Metal Foams. *J Porous Mater* **2009**, *16* (6), 675–681. https://doi.org/10.1007/s10934-008-9248-1.
(27) Griffith, M. L.; Halloran, J. W. Freeform Fabrication of Ceramics via Stereolithography. *Journal of the American Ceramic Society* **1996**, *79* (10), 2601–2608. https://doi.org/10.1111/j.1151-2916.1996.tb09022.x.
(28) Zakeri, S.; Vippola, M.; Levänen, E. A Comprehensive Review of the Photopolymerization of Ceramic Resins Used in Stereolithography. *Additive Manufacturing* **2020**, *35*, 101177. https://doi.org/10.1016/j.addma.2020.101177.
(29) Mangesana, N.; Mainza, A.; Govender, I.; Van der Westhuizen, A.; Narasimha, M. The Effect of Particle Sizes and Solids Concentration on the Rheology of Silica Sand Based Suspensions. *Journal of the Southern African Institute of Mining and Metallurgy* **2008**, *108*.
(30) Lobry, L.; Lemaire, E.; Blanc, F.; Gallier, S.; Peters, F. Shear Thinning in Non-Brownian Suspensions Explained by Variable Friction between Particles. *Journal of Fluid Mechanics* **2019**, 682–710. https://doi.org/10.1017/jfm.2018.881.
(31) Papadopoulou, A.; Gillissen, J. J.; Wilson, H. J.; Tiwari, M. K.; Balabani, S. On the Shear Thinning of Non-Brownian Suspensions: Friction or Adhesion? *Journal of Non-Newtonian Fluid Mechanics* **2020**, *281*, 104298. https://doi.org/10.1016/j.jnnfm.2020.104298.
(32) Mewis, J. Rheology of Suspensions. In *Rheology*; Astarita, G., Marrucci, G., Nicolais, L., Eds.; Springer US: Boston, MA, 1980; pp 149–168. https://doi.org/10.1007/978-1-4684-3740-9_10.
(33) Scalera, F.; Esposito Corcione, C.; Montagna, F.; Sannino, A.; Maffezzoli, A. Development and Characterization of UV Curable Epoxy/Hydroxyapatite Suspensions for Stereolithography Applied to Bone Tissue Engineering. *Ceramics International* **2014**, *40* (10), 15455–15462. https://doi.org/10.1016/j.ceramint.2014.06.117.
(34) Habib, E.; Wang, R.; Zhu, X. X. Correlation of Resin Viscosity and Monomer Conversion to Filler Particle Size in Dental Composites. *Dental Materials* **2018**, *34* (10), 1501–1508. https://doi.org/10.1016/j.dental.2018.06.008.
(35) Johnston, P. K.; Doyle, E.; Orzel, R. A. Acrylics: A Literature Review of Thermal Decomposition Products and Toxicity. *Journal of the American College of Toxicology* **1988**, *7* (2), 139–200. https://doi.org/10.3109/10915818809014519.
(36) Chattopadhyay, D. K.; Rohini Kumar, D. B.; Sreedhar, B.; Raju, K. V. S. N. Thermal Stability and Dynamic Mechanical Behavior of Acrylic Resin and Acrylic Melamine Coatings. *J. Appl. Polym. Sci.* **2004**, *91* (1), 27–34. https://doi.org/10.1002/app.13145.
(37) Bertini, F.; Audisio, G.; Zuev, V. V. Investigation on the Thermal Degradation of Poly-n-Alkyl Acrylates and Poly-n-Alkyl Methacrylates (C1–C12). *Polymer Degradation and Stability* **2005**, *89* (2), 233–239. https://doi.org/10.1016/j.polymdegradstab.2004.11.023.
(38) Konai, N.; Raidandi, D.; Pizzi, A.; Girods, P.; Lagel, M.-C.; Kple, M. Thermogravimetric Analysis of Anningre Tannin Resin. *Maderas, Cienc. tecnol.* **2016**, No. ahead, 0–0. https://doi.org/10.4067/S0718-221X2016005000022.

(39) Peyser, P.; Bascom, W. D. Effect of Filler and Cooling Rate on the Glass Transition of Polymers. *Journal of Macromolecular Science, Part B* **1977**, *13* (4), 597–610. https://doi.org/10.1080/00222347708212211.
(40) Hagita, K.; Morita, H. Effects of Polymer/Filler Interactions on Glass Transition Temperatures of Filler-Filled Polymer Nanocomposites. *Polymer* **2019**, *178*, 121615. https://doi.org/10.1016/j.polymer.2019.121615.
(41) Tondi, G.; Petutschnigg, A. Middle Infrared (ATR FT-MIR) Characterization of Industrial Tannin Extracts. *Industrial Crops and Products* **2015**, *65*, 422–428. https://doi.org/10.1016/j.indcrop.2014.11.005.
(42) Szczurek, A.; Martinez de Yuso, A.; Fierro, V.; Pizzi, A.; Celzard, A. Tannin-Based Monoliths from Emulsion-Templating. *Materials & Design* **2015**, *79*, 115–126. https://doi.org/10.1016/j.matdes.2015.04.020.
(43) Szczurek, A.; Fierro, V.; Pizzi, A.; Celzard, A. Mayonnaise, Whipped Cream and Meringue, a New Carbon Cuisine. *Carbon* **2013**, *58*, 245–248. https://doi.org/10.1016/j.carbon.2013.02.056.
(44) Szczurek, A.; Fierro, V.; Plyushch, A.; Macutkevic, J.; Kuzhir, P.; Celzard, A. Structure and Electromagnetic Properties of Cellular Glassy Carbon Monoliths with Controlled Cell Size. *Materials* **2018**, *11* (5), 709. https://doi.org/10.3390/ma11050709.
(45) Soukup, L.; Gregora, I.; Jastrabik, L.; Koňáková, A. Raman Spectra and Electrical Conductivity of Glassy Carbon. *Materials Science and Engineering: B* **1992**, *11* (1–4), 355–357. https://doi.org/10.1016/0921-5107(92)90240-A.
(46) Kuzhir, P.; Paddubskaya, A.; Bychanok, D.; Liubimau, A.; Ortona, A.; Fierro, V.; Celzard, A. 3D-Printed, Carbon-Based, Lossy Photonic Crystals: Is High Electrical Conductivity the Must? *Carbon* **2020**, *171*, 484–492. https://doi.org/10.1016/j.carbon.2020.09.020.

GRAPHICAL ABSTRACT

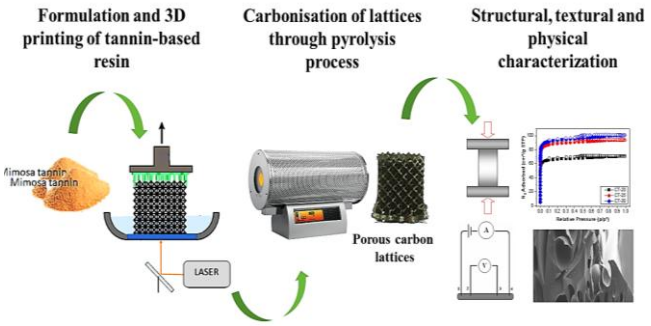

1 For Table of contents Use only

SYNOPSIS

Highly porous, conductive and mechanically resistant 3D-printed bio-based carbon were produced from tannin precursors through stereolithography.